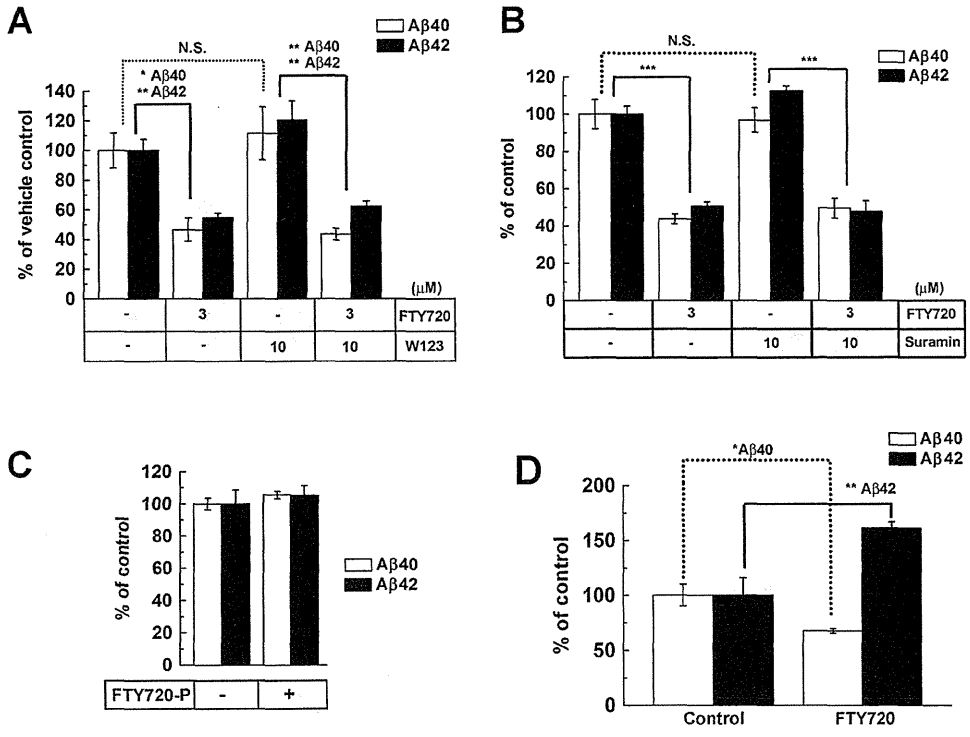

Figure 4. The effect of FTY720 on Aβ production is independent of downstream signaling of S1P receptors. (**A**) Levels of secreted Aβ from N2a cells co-treated with FTY720 and S1PR1 receptor antagonist W123 for 24 hrs (n = 4, mean ± SEM; *P<0.05, **P<0.01, N.S. no significant difference). (**B**) Levels of secreted Aβ from N2a cells co-treated with FTY720 and Gi protein inhibitor suramin for 24 hrs (n = 4, mean ± SEM; ***P<0.001, N.S. no significant difference). (**C**) Levels of secreted Aβ from N2a cells treated with FTY720-P for 24 hrs (n = 4, mean ± SEM). (**D**) *In vivo* effect of FTY720 on Aβ levels in AD model mice brain. Levels of soluble Aβ in the cerebral cortices of female A7 mice at 6 months of age after 6-days treatment with FTY720 (0.5 mg/kg/day, s.c.). Total brain human Aβ levels were measured by human-Aβ specific sandwich ELISA (n = 3–4, mean ± SEM, *P<0.05, ** p<0.01).
doi:10.1371/journal.pone.0064050.g004

the Aβ42 metabolism *in vivo* through altering the clearance of Aβ42 by microglial cells, overriding the inhibitory effects on neurons. As FTY720 has been approved for MS therapy in clinics, the regulatory mechanisms whereby S1PR modulators impact on Aβ42 metabolism, as well as on the inflammatory responses in AD brains, should further be characterized, in the light of therapeutics as well as adverse effects in humans. In sum, we identified a novel role of S1PR modulators on Aβ, which may open up a novel aspect in Aβ metabolism and lead to a novel therapeutic strategy for AD.

Supporting Information

Figure S1 AlamarBlue assay of N2aNH cells treated with S1PR modulators. After 24 hr treatment with S1PR modulators, N2aNH cells were incubated with cultured medium containing almarBlue (Invitrogen). Medium was collected to monitor fluorescence at 530–560/590 nm excitation/emission wavelengthes.
(TIF)

Figure S2 Effect of S1PR1 agonist and antagonist on ERK1/2 phosphorylation. Immunoblotting analysis of N2a cell lysates for ERK1/2 phosphorylation. Prior to stimulation with the indicated compounds, N2a cells were starved in serum free medium for 6 hr. Results of densitometric analysis of phosphorylated ERK1/2 (compared with control) are shown below the columns. (**A**) N2a cells were incubated for 10 min with the FTY720 (1 μM), FTY720-P (1 μM), SEW2871 (1 μM), and PKC activator PMA (Phorbol 12-Myristate 13-acetate; 1 μM), which in known as an activator of ERK1/2 phosphorylation. (**B**) N2a cells were preincubated with or without 1 μM W123 for 10 min. After addition of 1 μM SEW2871, cells were further incubated for 30 min and harvested for immunoblotting.
(TIF)

Figure S3 Dose dependent responses of S1PR1 agonist and antagonist on N2aNH cells. N2aNH cells were treated with SEW2871 or W123 for 24 hr at indicated doses. These reagents have no toxicity at 0.3, 1, 3, and 10 μM (**A**; alamarBlue assay), and failed to affect the Aβ40 production at indicated doses (**B**).
(TIF)

Acknowledgments

The authors are grateful to Drs. R. Kopan (Washington University in St. Louis) and J. Naslund (Karolinska Institutet in Sweden) for valuable reagents, Takeda pharmaceutical company for Aβ ELISA, and our current and previous laboratory members for helpful discussions and technical assistance.

Author Contributions

Conceived and designed the experiments: NT TT. Performed the experiments: NT TS IE SO HI. Analyzed the data: NT TT. Contributed reagents/materials/analysis tools: KT. Wrote the paper: NT TT TI.

References

1. Haughey NJ, Bandaru VV, Bae M, Mattson MP (2010) Roles for dysfunctional sphingolipid metabolism in Alzheimer's disease neuropathogenesis. Biochimica et biophysica acta 1801: 878–886.
2. Cutler RG, Kelly J, Storie K, Pedersen WA, Tammara A, et al. (2004) Involvement of oxidative stress-induced abnormalities in ceramide and cholesterol metabolism in brain aging and Alzheimer's disease. Proceedings of the National Academy of Sciences of the United States of America 101: 2070–2075.
3. Han X, D MH, McKeel DW, Jr., Kelley J, Morris JC (2002) Substantial sulfatide deficiency and ceramide elevation in very early Alzheimer's disease: potential role in disease pathogenesis. Journal of neurochemistry 82: 809–818.
4. He X, Huang Y, Li B, Gong CX, Schuchman EH (2010) Deregulation of sphingolipid metabolism in Alzheimer's disease. Neurobiology of aging 31: 398–408.
5. Grimm MO, Rothhaar TL, Hartmann T (2012) The role of APP proteolytic processing in lipid metabolism. Experimental brain research Experimentelle Hirnforschung Experimentation cerebrale 217: 365–375.
6. Tomita T (2009) Secretase inhibitors and modulators for Alzheimer's disease treatment. Expert review of neurotherapeutics 9: 661–679.
7. De Strooper B, Vassar R, Golde T (2010) The secretases: enzymes with therapeutic potential in Alzheimer disease. Nature reviews Neurology 6: 99–107.
8. Vassar R, Kovacs DM, Yan R, Wong PC (2009) The beta-secretase enzyme BACE in health and Alzheimer's disease: regulation, cell biology, function, and therapeutic potential. The Journal of neuroscience: the official journal of the Society for Neuroscience 29: 12787–12794.
9. Takasugi N, Tomita T, Hayashi I, Tsuruoka M, Niimura M, et al. (2003) The role of presenilin cofactors in the gamma-secretase complex. Nature 422: 438–441.
10. Vetrivel KS, Thinakaran G (2010) Membrane rafts in Alzheimer's disease beta-amyloid production. Biochimica et biophysica acta 1801: 860–867.
11. Kalvodova L, Kahya N, Schwille P, Ehehalt R, Verkade P, et al. (2005) Lipids as modulators of proteolytic activity of BACE: involvement of cholesterol, glycosphingolipids, and anionic phospholipids in vitro. The Journal of biological chemistry 280: 36815–36823.
12. Osenkowski P, Ye W, Wang R, Wolfe MS, Selkoe DJ (2008) Direct and potent regulation of gamma-secretase by its lipid microenvironment. The Journal of biological chemistry 283: 22529–22540.
13. Holmes O, Paturi S, Ye W, Wolfe MS, Selkoe DJ (2012) Effects of membrane lipids on the activity and processivity of purified gamma-secretase. Biochemistry 51: 3565–3575.
14. Brinkmann V, Billich A, Baumruker T, Heining P, Schmouder R, et al. (2010) Fingolimod (FTY720): discovery and development of an oral drug to treat multiple sclerosis. Nat Rev Drug Discov 9: 883–897.
15. Aktas O, Kury P, Kieseier B, Hartung HP (2010) Fingolimod is a potential novel therapy for multiple sclerosis. Nat Rev Neurol 6: 373–382.
16. Zemann B, Kinzel B, Muller M, Reuschel R, Mechtcheriakova D, et al. (2006) Sphingosine kinase type 2 is essential for lymphopenia induced by the immunomodulatory drug FTY720. Blood 107: 1454–1458.
17. Don AS, Martinez-Lamenca C, Webb WR, Proia RL, Roberts E, et al. (2007) Essential requirement for sphingosine kinase 2 in a sphingolipid apoptosis pathway activated by FTY720 analogues. J Biol Chem 282: 15833–15842.
18. Hogenauer K, Billich A, Pally C, Streiff M, Wagner T, et al. (2008) Phosphorylation by sphingosine kinase 2 is essential for in vivo potency of FTY720 analogues. ChemMedChem 3: 1027–1029.
19. Foster CA, Howard LM, Schweitzer A, Persohn E, Hiestand PC, et al. (2007) Brain penetration of the oral immunomodulatory drug FTY720 and its phosphorylation in the central nervous system during experimental autoimmune encephalomyelitis: consequences for mode of action in multiple sclerosis. J Pharmacol Exp Ther 323: 469–475.
20. Choi JW, Gardell SE, Herr DR, Rivera R, Lee CW, et al. (2011) FTY720 (fingolimod) efficacy in an animal model of multiple sclerosis requires astrocyte sphingosine 1-phosphate receptor 1 (S1P1) modulation. Proceedings of the National Academy of Sciences of the United States of America 108: 751–756.
21. Fujino M, Funeshima N, Kitazawa Y, Kimura H, Amemiya H, et al. (2003) Amelioration of experimental autoimmune encephalomyelitis in Lewis rats by FTY720 treatment. The Journal of pharmacology and experimental therapeutics 305: 70–77.
22. Takasugi N, Sasaki T, Suzuki K, Osawa S, Isshiki H, et al. (2011) BACE1 Activity Is Modulated by Cell-Associated Sphingosine-1-Phosphate. The Journal of neuroscience: the official journal of the Society for Neuroscience 31: 6850–6857.
23. Kaneko T, Murakami T, Kawana H, Takahashi M, Yasue T, et al. (2006) Sphingosine-1-phosphate receptor agonists suppress concanavalin A-induced hepatic injury in mice. Biochemical and biophysical research communications 345: 85–92.
24. Kan T, Tominari Y, Morohashi Y, Natsugari H, Tomita T, et al. (2003) Solid-phase synthesis of photoaffinity probes: highly efficient incorporation of biotin-tag and cross-linking groups. Chemical communications: 2244–2245.
25. Tomita T, Takikawa R, Koyama A, Morohashi Y, Takasugi N, et al. (1999) C terminus of presenilin is required for overproduction of amyloidogenic Abeta42 through stabilization and endoproteolysis of presenilin. The Journal of neuroscience: the official journal of the Society for Neuroscience 19: 10627–10634.
26. Tomita T, Maruyama K, Saido TC, Kume H, Shinozaki K, et al. (1997) The presenilin 2 mutation (N141I) linked to familial Alzheimer disease (Volga German families) increases the secretion of amyloid beta protein ending at the 42nd (or 43rd) residue. Proceedings of the National Academy of Sciences of the United States of America 94: 2025–2030.
27. Iwatsubo T, Odaka A, Suzuki N, Mizusawa H, Nukina N, et al. (1994) Visualization of A beta 42(43) and A beta 40 in senile plaques with end-specific A beta monoclonals: evidence that an initially deposited species is A beta 42(43). Neuron 13: 45–53.
28. Qi-Takahara Y, Morishima-Kawashima M, Tanimura Y, Dolios G, Hirotani N, et al. (2005) Longer forms of amyloid beta protein: implications for the mechanism of intramembrane cleavage by gamma-secretase. The Journal of neuroscience: the official journal of the Society for Neuroscience 25: 436–445.
29. Merhi A, Andre B (2012) Internal amino acids promote Gap1 permease ubiquitylation via TORC1/Npr1/14-3-3-dependent control of the Bul arrestin-like adaptors. Mol Cell Biol 32: 4510–4522.
30. Kopan R, Schroeter EH, Weintraub H, Nye JS (1996) Signal transduction by activated mNotch: importance of proteolytic processing and its regulation by the extracellular domain. Proceedings of the National Academy of Sciences of the United States of America 93: 1683–1688.
31. Iwata H, Tomita T, Maruyama K, Iwatsubo T (2001) Subcellular compartment and molecular subdomain of beta-amyloid precursor protein relevant to the Abeta 42-promoting effects of Alzheimer mutant presenilin 2. The Journal of biological chemistry 276: 21678–21685.
32. Imamura Y, Watanabe N, Umezawa N, Iwatsubo T, Kato N, et al. (2009) Inhibition of gamma-secretase activity by helical beta-peptide foldamers. Journal of the American Chemical Society 131: 7353–7359.
33. Becuwe M, Herrador A, Haguenauer-Tsapis R, Vincent O, Leon S (2012) Ubiquitin-mediated regulation of endocytosis by proteins of the arrestin family. Biochem Res Int 2012: 242764.
34. Fukumoto H, Tomita T, Matsunaga H, Ishibashi Y, Saido TC, et al. (1999) Primary cultures of neuronal and non-neuronal rat brain cells secrete similar proportions of amyloid beta peptides ending at A beta40 and A beta42. Neuroreport 10: 2965–2969.
35. Suzuki K, Hayashi Y, Nakahara S, Kumazaki H, Prox J, et al. (2012) Activity-dependent proteolytic cleavage of neuroligin-1. Neuron 76: 410–422.
36. Karlstrom H, Bergman A, Lendahl U, Naslund J, Lundkvist J (2002) A sensitive and quantitative assay for measuring cleavage of presenilin substrates. The Journal of biological chemistry 277: 6763–6766.
37. Yamada K, Yabuki C, Seubert P, Schenk D, Hori Y, et al. (2009) Abeta immunotherapy: intracerebral sequestration of Abeta by an anti-Abeta monoclonal antibody 266 with high affinity to soluble Abeta. The Journal of neuroscience: the official journal of the Society for Neuroscience 29: 11393–11398.
38. Takabe K, Paugh SW, Milstien S, Spiegel S (2008) "Inside-out" signaling of sphingosine-1-phosphate: therapeutic targets. Pharmacol Rev 60: 181–195.
39. Lee MJ, Evans M, Hla T (1996) The inducible G protein-coupled receptor edg-1 signals via the G(i)/mitogen-activated protein kinase pathway. The Journal of biological chemistry 271: 11272–11279.
40. Mullershausen F, Craveiro LM, Shin Y, Cortes-Cros M, Bassilana F, et al. (2007) Phosphorylated FTY720 promotes astrocyte migration through sphingosine-1-phosphate receptors. Journal of neurochemistry 102: 1151–1161.
41. Wei SH, Rosen H, Matheu MP, Sanna MG, Wang SK, et al. (2005) Sphingosine 1-phosphate type 1 receptor agonism inhibits transendothelial migration of medullary T cells to lymphatic sinuses. Nature immunology 6: 1228–1235.
42. Miron VE, Jung CG, Kim HJ, Kennedy TE, Soliven B, et al. (2008) FTY720 modulates human oligodendrocyte progenitor process extension and survival. Ann Neurol 63: 61–71.
43. Ni Y, Zhao X, Bao G, Zou L, Teng L, et al. (2006) Activation of beta2-adrenergic receptor stimulates gamma-secretase activity and accelerates amyloid plaque formation. Nat Med 12: 1390–1396.
44. Tanaka S, Ishii K, Kasai K, Yoon SO, Saeki Y (2007) Neural expression of G protein-coupled receptors GPR3, GPR6, and GPR12 up-regulates cyclic AMP levels and promotes neurite outgrowth. J Biol Chem 282: 10506–10515.
45. Thathiah A, Spittaels K, Hoffmann M, Staes M, Cohen A, et al. (2009) The orphan G protein-coupled receptor 3 modulates amyloid-beta peptide generation in neurons. Science 323: 946–951.
46. Liu X, Zhao X, Zeng X, Bossers K, Swaab DF, et al. (2012) beta-Arrestin1 regulates gamma-secretase complex assembly and modulates amyloid-beta pathology. Cell Res.
47. Thathiah A, Horre K, Snellinx A, Vandewyer E, Huang Y, et al. (2012) beta-arrestin 2 regulates Abeta generation and gamma-secretase activity in Alzheimer's disease. Nat Med.
48. Lieven CJ, Ribich JD, Crowe ME, Levin LA (2012) Redox proteomic identification of visual arrestin dimerization in photoreceptor degeneration after photic injury. Invest Ophthalmol Vis Sci 53: 3990–3998.

49. Osawa S, Funamoto S, Nobuhara M, Wada-Kakuda S, Shimojo M, et al. (2008) Phosphoinositides suppress gamma-secretase in both the detergent-soluble and -insoluble states. J Biol Chem 283: 19283–19292.
50. Gomez-Raja J, Davis DA (2012) The beta-arrestin-like protein Rim8 is hyperphosphorylated and complexes with Rim21 and Rim101 to promote adaptation to neutral-alkaline pH. Eukaryot Cell 11: 683–693.
51. Shichita T, Sugiyama Y, Ooboshi H, Sugimori H, Nakagawa R, et al. (2009) Pivotal role of cerebral interleukin-17-producing gammadeltaT cells in the delayed phase of ischemic brain injury. Nature medicine 15: 946–950.
52. Kaneider NC, Lindner J, Feistritzer C, Sturn DH, Mosheimer BA, et al. (2004) The immune modulator FTY720 targets sphingosine-kinase-dependent migration of human monocytes in response to amyloid beta-protein and its precursor. FASEB J 18: 1309–1311.

Medical Physics
The International Journal of Medical Physics Research and Practice

Improved volumetric measurement of brain structure with a distortion correction procedure using an ADNI phantom

Norihide Maikusa, Fumio Yamashita, Kenichiro Tanaka, Osamu Abe, Atsushi Kawaguchi, Hiroyuki Kabasawa, Shoma Chiba, Akihiro Kasahara, Nobuhisa Kobayashi, Tetsuya Yuasa, Noriko Sato, Hiroshi Matsuda, Takeshi Iwatsubo, and The Japanese Alzheimer's Disease Neuroimaging Initiative

Citation: Medical Physics **40**, 062303 (2013); doi: 10.1118/1.4801913
View online: http://dx.doi.org/10.1118/1.4801913
View Table of Contents: http://scitation.aip.org/content/aapm/journal/medphys/40/6?ver=pdfcov
Published by the American Association of Physicists in Medicine

Improved volumetric measurement of brain structure with a distortion correction procedure using an ADNI phantom

Norihide Maikusa[a)]
Integrative Brain Imaging Center, National Center of Neurology and Psychiatry, Tokyo 187-855, Japan

Fumio Yamashita
Iwate Medical University, Morioka 028-3694, Japan

Kenichiro Tanaka
Research Association for Biotechnology, Tokyo 105-0003, Japan

Osamu Abe
Department of Radiology, Nihon University School of Medicine, Tokyo 173-8610, Japan

Atsushi Kawaguchi
Biostatistics Center, Kurume University, Kurume 830-0011, Japan

Hiroyuki Kabasawa
Applied Science Laboratory, GE Healthcare, Tokyo 191-8503, Japan

Shoma Chiba
Research Association for Biotechnology, Tokyo 105-0003, Japan

Akihiro Kasahara
Imaging Center, The University of Tokyo Hospital, Tokyo 113-8655, Japan

Nobuhisa Kobayashi
Oizumi Hospital, Tokyo 178-0061, Japan

Tetsuya Yuasa
Department of Bio-systems Engineering, Graduate School of Science and Engineering, Yamagata University, Yonezawa 992-8510, Japan

Noriko Sato
Department of Radiology, National Center of Neurology and Psychiatry, Tokyo 187-855, Japan

Hiroshi Matsuda
Integrative Brain Imaging Center, National Center of Neurology and Psychiatry, Tokyo 187-855, Japan

Takeshi Iwatsubo
Department of Neuropathology, Graduate School of Medicine, The University of Tokyo, Tokyo 113-0033, Japan

The Japanese Alzheimer's Disease Neuroimaging Initiative

(Received 23 August 2012; revised 1 April 2013; accepted for publication 2 April 2013; published 28 May 2013)

Purpose: Serial magnetic resonance imaging (MRI) images acquired from multisite and multivendor MRI scanners are widely used in measuring longitudinal structural changes in the brain. Precise and accurate measurements are important in understanding the natural progression of neurodegenerative disorders such as Alzheimer's disease. However, geometric distortions in MRI images decrease the accuracy and precision of volumetric or morphometric measurements. To solve this problem, the authors suggest a commercially available phantom-based distortion correction method that accommodates the variation in geometric distortion within MRI images obtained with multivendor MRI scanners.

Methods: The authors' method is based on image warping using a polynomial function. The method detects fiducial points within a phantom image using phantom analysis software developed by the Mayo Clinic and calculates warping functions for distortion correction. To quantify the effectiveness of the authors' method, the authors corrected phantom images obtained from multivendor MRI scanners and calculated the root-mean-square (RMS) of fiducial errors and the circularity ratio as evaluation values. The authors also compared the performance of the authors' method with that of a distortion correction method based on a spherical harmonics description of the generic gradient design parameters. Moreover, the authors evaluated whether this correction improves the test–retest reproducibility of voxel-based morphometry in human studies.

Results: A Wilcoxon signed-rank test with uncorrected and corrected images was performed. The root-mean-square errors and circularity ratios for all slices significantly improved ($p < 0.0001$)

after the authors' distortion correction. Additionally, the authors' method was significantly better than a distortion correction method based on a description of spherical harmonics in improving the distortion of root-mean-square errors ($p < 0.001$ and 0.0337, respectively). Moreover, the authors' method reduced the RMS error arising from gradient nonlinearity more than gradwarp methods. In human studies, the coefficient of variation of voxel-based morphometry analysis of the whole brain improved significantly from 3.46% to 2.70% after distortion correction of the whole gray matter using the authors' method (Wilcoxon signed-rank test, $p < 0.05$).

Conclusions: The authors proposed a phantom-based distortion correction method to improve reproducibility in longitudinal structural brain analysis using multivendor MRI. The authors evaluated the authors' method for phantom images in terms of two geometrical values and for human images in terms of test–retest reproducibility. The results showed that distortion was corrected significantly using the authors' method. In human studies, the reproducibility of voxel-based morphometry analysis for the whole gray matter significantly improved after distortion correction using the authors' method.
 [http://dx.doi.org/10.1118/1.4801913]

Key words: Alzheimer's disease, magnetic resonance imaging, geometric distortion, image normalization

I. INTRODUCTION

Alzheimer's disease (AD) is the most common cause of dementia, and typically shows memory impairment at the earliest clinical stage. Magnetic resonance imaging (MRI) has shown much promise as a biomarker method of quantifying AD progression. Use of MRI in morphometric or volumetric measurement of brain atrophy, such as changes in cortical thickness, hippocampus volume, whole brain volume, voxel-based morphometry, or tensor-based morphometry, has resulted in improved diagnosis.[1–9] These measurements can also be used to assess the effectiveness of applied therapies.[10–12] A large multisite longitudinal study named the Alzheimer's Disease Neuroimaging Initiative (ADNI) was launched in the United States (US) in 2005.[13] A goal of the US-ADNI is to validate the MRI scan as a surrogate marker of AD. The Japanese Alzheimer's Disease Neuroimaging Initiative (J-ADNI) is another large multisite imaging study with the same goals as the US-ADNI.[14] Following the ADNI's study protocols, the J-ADNI recruited 150 elderly controls, 300 subjects with mild cognitive impairment, and 150 AD patients. Three-dimensional T1-weighted images were acquired from subjects and a specifically designed ADNI phantom (Phantom Laboratory, Salem, New York) was used to inspect image quality and artifacts as well as the stability of acquisitions.

MRI scans often contain geometrical distortions. The most prominent factors are image gradient nonlinearity, static magnetic field inhomogeneity, and magnetic susceptibility as typical image reconstruction relies on linear approximation of a magnetic field gradient.[15] A distortion can cause a superficial local volume change, which affects the precision and accuracy of volumetric and morphometric analysis.[13,15–19] The US-ADNI corrects image geometry for gradient nonlinearity using the gradwarp (GW) correction, which involves a gradient coil design and a phantom-based scaling correction method.[13,15] The former relies on the geometry of gradient coil construction and can only correct the nonlinear component of geometrical distortion. The latter corrects linear scaling changes of images through an affine transformation of nine degrees of freedom. However, GW correction requires information of the coil construction; the scanner is limited if this information is not available. Additionally, GW correction does not correct distortion variability between scanners or changes because of aging within the same scanner, and requires prior information of the gradient coil construction from the manufacture and is not available for all scanners.

On the other hand, several phantom-based distortion-correction methods have been reported in the literature.[16,17,20–22] Baldwin *et al.* characterized and corrected distortion using a three-dimensional (3D) grid phantom and elastic-body spline-kernel transformation function.[17] Carmanos *et al.* constructed a DUPLO-based phantom and proposed distortion correction using information characterized by that phantom and spherical harmonic expansion.[16] Schad *et al.*[20] carried out an early investigation on two-dimensional (2D) MRI distortion correction using a 2D polynomial equation. Menuel *et al.*[22] used phantom including cylindrical rods as fiducial points. Langlois *et al.* proposed a correction method based on the Fourier transform and a simple cubic phantom.[21] This method obtained information about distortion to allow correction of both gradient nonlinearity and background field inhomogeneity for many subsequent patients via scans of a phantom of well-known geometry. However, Gunter *et al.* reported that the distortion factor drifts.[19] Therefore, in a phantom-based method, it is desirable to periodically scan the phantom to correct the drift. The above studies used the phantom only to assess characteristics of the geometrical distortion.

In J-ADNI MRI scanning protocol, ADNI phantom images are acquired consecutively after patients are scanned in accordance with the US-ADNI protocol.[13] The ADNI phantom image was used to check the signal-to-noise ratio (SNR), contrast, and geometric distortion for all subjects at each scan time as done by the US-ADNI. Gunter reported that an ADNI phantom can be measured in a multisite study to identify scanner errors through central monitoring, and in the latest result, these errors would have contributed to imprecision in quantitative metrics of more than 25%.[19] The present report states

TABLE I. Range of parameters for MRI acquisition of human subjects and phantoms.

Manufacturer	Model name	Slice num	TR[a] (ms)	TI (ms)	Flip (deg)	Matrix [in-plane resolution (mm^2)]	Fov (mm^2)	Slice thickness (mm)	Plane
GE	GENESIS SIGNA SIGNA EXCITE SIGNA HDx/HDxt	166–180							
Siemens	Avanto MAGNETOM VISION Sonata Symphony Symphony Vision Symphony Tim	160	MA[b]:2400 BC[c]:3000	1000	8	192×192 [1.25×1.25] or 256×256 [0.9375×0.9375]	240×240	Human: 1.2 Phantom 1.3	Sagittal PE[d] = A/P
Toshiba	Excelart Vantage	180							
Philips	Achieva Intera	170	MA:2300						
Hitachi	ECHELON Vega	170	MA:2600	1100					

[a]TR is defined here as the receptition time for the inversion pulses.
[b]MA = multicoil phased-array head coil.
[c]BC = birdcage or volume head coil.
[d]PE is the phase encoding direction.

that ADNI phantom measurement is necessary to ensure consistency of MRI data acquired in a multisite longitudinal study like the ADNI project. If the distortion can be corrected using an ADNI phantom image, the correction can be applied to the ADNI protocol using the ADNI phantom that was already being employed for other purposes. In other words, the ADNI phantom-based distortion correction method can serve dual purposes: correction of geometrical distortion and monitoring of the scanner condition.

For the reason above, we suggest an ADNI phantom-based distortion correction using a polynomial equation to enhance the reliability and accuracy of structural analysis of brain images. Our method can correct nonlinear and linear components of geometrical distortion using the polynomial function. ADNI phantom scanning is available commercially and is recommended to monitor several MRI scanner conditions in multisite and longitudinal studies compliant with the ADNI study protocol. In this paper, we refer to this correction as the J-ADNI method. We evaluate the effectiveness of the method in terms of fiducial errors and circularity in phantom studies. For human studies, we use voxel-based morphometry (VBM). Finally, we compare improvements in distortion correction. Our method uses a commercially available phantom, and therefore attains distortion correction for all scanners without requiring information of the coil design from the manufacturer.

II. METHODS

II.A. MRI data and protocols

The pulse sequence used to acquire 3D, 1.5-T T1-weighted images was the magnetization-prepared rapid gradient echo (MPRAGE) sequence. MRI scanners were accepted via checking conformance with J-ADNI protocols, and we checked whether any image suffered serious degradation due to a motion artifact, warping around into the side of the skull, low SNR, signal loss, or metal artifact. This strengthened the longitudinal and cross-sectional analysis. The MPRAGE sequence is used to enhance gray/white contrast to noise for superior performance in applications requiring cortical segmentation.[13] We thus introduced the MPRAGE sequence to acquire magnetic resonance images in the J-ADNI. The parameters used to obtain magnetic resonance images with the MPRAGE sequence are listed in Table I for each manufacturer and model. For Siemens Magnetom Vision, Toshiba Excelart Vantage, and Hitachi Echelon Vega systems, a customized sequence designed to retain compatibility with the ADNI MPRAGE sequence was used. The parameters were chosen to be as close as possible to the parameters of the US-ADNI's MRI sequence to merge MRI data for global analysis and/or comparison of the population at a future date.

II.B. ADNI phantom design

The ADNI phantom contains 165 polycarbonate spheres filled with copper sulfate inside a water-filled clear urethane shell (20 cm in diameter). Four contrast spheres (3.0 cm in diameter) with copper sulfate concentrations of 0.9, 1.2, 1.7, and 2.4 mM provided scanner contrast. A large sphere (6.0 cm in diameter) containing 3.3 mM copper sulfate solution at the center of the phantom was used to calculate the SNR of a scanner and define the origin of the coordinate system. Inclusions (158 with diameters of 1.0 cm, and two with diameters of 1.5 cm) in 3.3 mM copper sulfate solutions, known as fiducial or small spheres, defined the geometrical coordinates of the phantom image in addition to

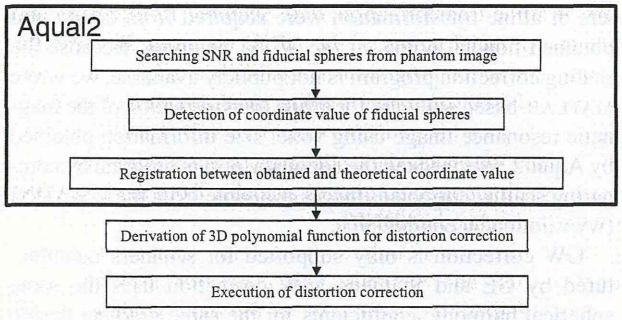

FIG. 1. Flowchart of distortion correction including mass-preservation resampling.

the SNR sphere. The phantom (Phantom Laboratory) was manufactured via numerous inspections of batches of both machined and molded components along with assembly inspections. The tolerance for the sphere locations was ±0.125 mm in the phantom's x–y directions (parallel to the equatorial plane) and ±0.3 mm in the z direction.

II.C. Method for correcting phantom-based geometrical distortion

A flow chart of the proposed distortion correction method is shown in Fig. 1. First, we performed phantom image analysis using Aqual2 (Acceptance Qualification tool), which was developed at the Mayo Clinic.[19] Aqual2 was written in MATLAB (MathWorks, Natick, Massachusetts) and is available via the Internet (http://adni.loni.ucla.edu/research/research-tools/aqual2/). This program finds 160 fiducial spheres and a SNR sphere to obtain coordinate values relative to the center of phantom images. The program is then able to register the obtained and designed coordinate values. By comparing the actual measured coordinate value of the fiducial and SNR spheres with the designed coordinate value, we can calculate the distortion field of the scanner. The warping function from a distorted coordinate to a design (i.e., nondistorted) coordinate value is given by

$$\begin{cases} X = \sum \sum_{p+q+r\le n} \sum a_{pqr} x^p y^q z^r + \varepsilon \\ Y = \sum \sum_{p+q+r\le n} \sum b_{pqr} x^p y^q z^r + \varepsilon \\ Z = \sum \sum_{p+q+r\le n} \sum c_{pqr} x^p y^q z^r + \varepsilon \end{cases}, \quad (1)$$

where x, y, z and X, Y, Z are the obtained and designed coordinate values, respectively, along three orthogonal dimensions; p, q, and r are orders of the polynomial equation and n is the polynomial degree of a function; a_{pqr}, b_{pqr}, and c_{pqr} are coefficients of the polynomial equation; and ε is a Gaussian random variable. Because designed coordinate values of fiducial and SNR spheres are known, fiducial errors between design and obtained coordinate values reflect the geometric distortion of the scanner due to gradient nonlinearity, background field inhomogeneity, and magnetic susceptibility. We assume that the contribution of susceptibility in the ADNI phantom image is negligible. Thus, we can correct distortion in a MRI brain image for the same scanner using the equation derived from the phantom image. Note that our correction model has Gaussian distribution errors as described by ε in Eq. (1). Polynomial coefficients, a_{pqr}, b_{pqr}, and c_{pqr}, are calculated from the correspondence between x, y, z and X, Y, Z using Gaussian elimination to minimize Gaussian random variables in each of the three directions. Moreover, to use this polynomial equation, we must decide on the degrees of the polynomial (i.e., p, q, and r). To solve this problem, we use the Bayesian information criterion (BIC). The BIC is a criterion for model selection among a class of parametric models with different numbers of parameters.[23,24] In the present model, we assumed error variance between obtained and design sphere coordinate values given by a Gaussian distribution. The BIC is defined as

$$\mathrm{BIC}(n) = n \cdot \ln(\hat{\sigma}_e^2) + k \cdot \ln(n), \quad (2)$$

where σ is the error variance, n is the number of data points (i.e., the number of fiducial spheres), and k is the number of free parameters to be estimated. The best parameter of the polynomial equation is the one that minimizes Eq. (2). Hence, we selected an optimized set of polynomial functions for the three directions individually.

The polynomial function corrects geometrical distortion in a brain image, which is acquired immediately before phantom scanning with the same scanner. The resampling method used when an image is deformed to correct geometric distortion is trilinear interpolation. Additionally, it is necessary to correct the intensity to compensate for the change in effective voxel size with distortion. This intensity is corrected by multiplying the image intensity and the Jacobian determinant, $|J|$, calculated from the transformation equation at each voxel.[15,25] This equation is the polynomial function. We can calculate the Jacobian determinant, $|J|$, of the polynomial function associated with Eq. (1) as

$$|J| = \begin{vmatrix} \frac{\partial X'}{\partial x} & \frac{\partial X'}{\partial y} & \frac{\partial X'}{\partial z} \\ \frac{\partial Y'}{\partial x} & \frac{\partial Y'}{\partial y} & \frac{\partial Y'}{\partial z} \\ \frac{\partial Z'}{\partial x} & \frac{\partial Z'}{\partial y} & \frac{\partial Z'}{\partial z} \end{vmatrix}, \quad (3)$$

where $\partial/\partial x$, $\partial/\partial y$, and $\partial/\partial z$ are the partial derivative operators with respect to the orthogonal components, and X', Y', and Z' are the coordinates corrected by polynomial functions.

This correction software, written in MATLAB, executes automatically in about 15 min on a Xeon Processor E5540 (2.53 GHz) with RedHat Enterprise Linux 5.3 as the operating system using only input from phantom and brain images.

II.D. Evaluation metrics

For quantitative assessment of our correction method for phantom images acquired by all scanners ($n = 41$) at 38 J-ADNI clinical sites, we used two functions. The first function

was the root mean square (RMS) error in the determined location of fiducial spheres. The second function was the circularity ratio (CR) of an outer shell in a phantom image for three slices: axial, coronal, and sagittal. Polynomial functions for the correction procedure obtained from one phantom image were used to deform other phantom images acquired 1 week later by the same scanner.

To obtain RMS errors, coordinate values of fiducial spheres were acquired from uncorrected and corrected phantom images using Aqual2. We compared obtained and designed coordinate values, and calculated RMS errors of fiducial spheres.

Our method used geometrical information of the positions of fiducial spheres in phantom images. Therefore, it was expected that our method corrects distortion around the fiducial spheres. The overfitting of the distortion correction is not as great as predicted; accordingly, RMS errors are less than expected but the whole-image structures have unforeseen shapes. To assess the adequacy of the image obtained after distortion correction around fiducial points, we used the CR metric. The CR is defined as the amount of geometrical circle distortion according to Japanese industrial standards. The outer shell of a phantom is spherical and its orthogonal plane images are thus truly circular. Therefore, CRs of the outer shell in axial, coronal, and sagittal slices were used as other metrics to assess distortion. The CR is useful in assessing the validity of our method outside the fiducial sphere. The CR can be calculated as

$$\mathrm{CR} = \frac{r_i}{r_c}, \tag{4}$$

where r_i and r_c are radii of the incircle and circumcircle, respectively. If the ratio of the radii of the two concentric circles (incircle and circumcircle) is 1.0, the boundary is a true circle. To calculate the CR, we draw an incircle and circumcircle manually in three orthogonal images (i.e., the axial, sagittal, and coronal images) with origins at the center of the 3D phantom image. An operator carried out this task after only being instructed to draw two circles inscribed and circumscribed on the boundary between the outer shell of the phantom and background. To demonstrate the performance of our method, the Wilcoxon signed-rank test was performed for uncorrected and corrected images because the data may not be normally distributed because of the small sample size. A two-sided p-value less than 0.05 was considered statistically significant.

II.E. Comparison of geometrical distortion correction methods of the J-ADNI and US-ADNI

The US-ADNI employs the GW correction method[13] and ADNI phantom-based scaling correction. In GW correction, a set of spherical harmonic coefficients is computed for a particular gradient coil design, and can be used to correct the distortion arising from gradient nonlinearity embedded in acquired images.[18,25] Moreover, ADNI phantom-based linear scaling correction involves reducing the observed geometric drift or voxel size adjustment employing an affine transformation of nine degrees of freedom.[19] The parameters of affine transformation were acquired from design and obtained fiducial points of the ADNI phantom. Because the scaling correction program is not publicly available, we wrote MATLAB-based software for affine transformation of the magnetic resonance image using voxel size information obtained by Aqual2. We checked the adequacy of this program by comparing scaling corrected images available from the US-ADNI (www.loni.ucla.edu/ADNI/).

GW correction is only supported for scanners manufactured by GE and Siemens. GW correction uses the same spherical harmonic coefficients for the same gradient design to correct distortion only arising from gradient nonlinearity. Therefore, it cannot correct distortion variations between scanners of the same model or changes with time for the same scanner. These variations are generated by machine maintenance, such as magnetic field adjustment, repair of the magnetic coil, and quenching. We compared our proposed correction method with the GW method and the GW-plus-scaling method for corrected phantom images. Here, we need to separate out the contribution of gradient nonlinearity from other distortion components because our method corrects inhomogeneity in the magnetic background field as well as gradient nonlinearity. Bakker *et al.* reported that distortion only arose from gradient nonlinearity in the phase-encoding direction in a two-dimensional magnetic resonance image.[26] Subsequently, Baldwin *et al.* reported that the slice-encoding direction as well as the phase-encoding direction provides distortion when this principle is extended to a 3D magnetic resonance image.[17] Here, we assess RMS errors along the phase- and slice-encoding directions (i.e., the A/P and R/L directions, respectively), and also the CR in the axial image to compare the efficacy of our method with that of the GW and GW-plus-scaling correction procedures.

GW software is publicly available to researchers and we were able to obtain gradient information from GE Healthcare Japan, but we could only correct images acquired by GE MRI scanners using GW. For a statistical comparison of the J-ADNI, GW, and GW-plus-scaling correction methods, a Steel–Dwass signed-rank test was performed for the RMS error and CR.

II.F. Application of the distortion correction method to human studies

Geometrical distortion is induced by background field inhomogeneity and magnetic susceptibility as well as gradient nonlinearity. Magnetic susceptibility is dependent on the imaged object. Our method assumes that the contribution of susceptibility to geometrical distortion of the ADNI phantom image is negligible. Therefore, to evaluate our simple and practical method of correcting images of human subjects, we performed VBM analysis using software developed by Matsuda *et al.*[8] This approach allows us to automatically detect early specific atrophy in AD using three-dimensional T1-weighted MRI data as a series of segmentations using statistical parametric mapping 8 (SPM8) with the toolbox DARTEL. The following is a brief explanation of the procedure. Gray/white matter can be anatomically segmented employing

a unified tissue-segmentation procedure after correction of image-intensity nonuniformity. Segmented images are then normalized to the MNI (Montreal Neurological Institute) space via a nonlinear transformation to a customized template created by DARTEL, modulation by the Jacobian determinant, and linear transformation from the customized template to MNI space. Finally, the images are smoothed using an 8-mm full-width-at-half-maximum Gaussian kernel. To perform Z-score analysis for gray matter, brain images of 80 healthy control volunteers without memory impairment or cognitive disorders (37 men and 43 women, 70.4 ± 7.8 years of age) were processed using the above procedures, and the mean and standard deviation of these smoothed modulated intensity values were calculated voxel by voxel in MNI space, preliminarily. Finally, a Z-score map was generated by comparing an individual image with a control mean and standard deviation at each voxel in a gray/white matter image. The Z-score was calculated as [control mean] − [individual value]/(control SD) and it shows atrophy relative to the normal control.

Directly assessing the usefulness of VBM analysis is difficult because the true brain atrophy of the subject is unknown. Therefore, we assumed that geometric distortion reduces the reproducibility of the Z-score. Segmentation and anatomical standardization errors may be increased by an anatomical volume change and partial volume effects resulting from distortion. We assessed the reproducibility of VBM analysis for brain images corrected using the J-ADNI method for 38 healthy volunteers (32 men and six women, 33.6 ± 10.7 years of age) scanned twice at an interval of 1 week. The phantom image was obtained immediately after each volunteer was scanned and the imaging sequence is identical with phantom scanning as described in Table I. Using the automated VBM software, we obtained two indicators for characterizing atrophy in medial temporal structures and in the whole brain.[8] The first indicator was the averaged Z-score in the medial temporal structures, which indicates the severity of atrophy in the entorhinal cortex and hippocampus. The second indicator was the extent of significant atrophy in the region of the whole brain, essentially the percentage of coordinates with a Z-score exceeding a threshold value (2.0) in the entire brain. We defined reproducibility as a coefficient of variation (CV) for these two indicators between the first and second scans.

III. RESULTS

III.A. Phantom studies

All phantom images were acquired with MRI scanners approved by the J-ADNI at 38 clinical sites. Polynomial functions were determined from phantom images acquired at week 0 and applied to other phantom images acquired by the same scanner 1 week later. The polynomial function was of third order along the A/P and R/L directions, and second order along the S/I direction. RMS errors of corrected phantom images obtained using a fourth- or fifth-order polynomial function vary less than RMS errors for the result obtained using a polynomial function of third order.

The resulting uncorrected images and images corrected using the J-ADNI, GW, and GW-plus-scaling correction methods are shown in Fig. 2. A red circle and yellow circle are superimposed on the outer and inner edges of the phantom shell, respectively. In the figure, although the outline of a phantom should be spherical, uncorrected and corrected GW phantom images are not circular. However, the outline of a corrected phantom image subject to the J-ADNI method appears to be circular. An example of the spatial distribution of fiducial sphere errors in a corresponding phantom image is shown in Fig. 3. Error levels corresponding to fiducial sphere positions are indicated by arrows of different color. A red arrow indicates errors over 3 mm, yellow indicates errors of 2–3 mm, blue indicates errors of 1–2 mm, and gray indicates errors of 0–1 mm. The direction of the arrow indicates the direction of the highest error at the orthogonal coordinate. Figures 3(b) and 3(c) show remaining errors over 1.0 mm at positions of designed fiducial spheres. However, the result of the J-ADNI method shows the errors of fiducial spheres under a voxel resolution of 1.0 mm. Therefore, the results show that our distortion correction method is qualitatively more efficient than other correction methods.

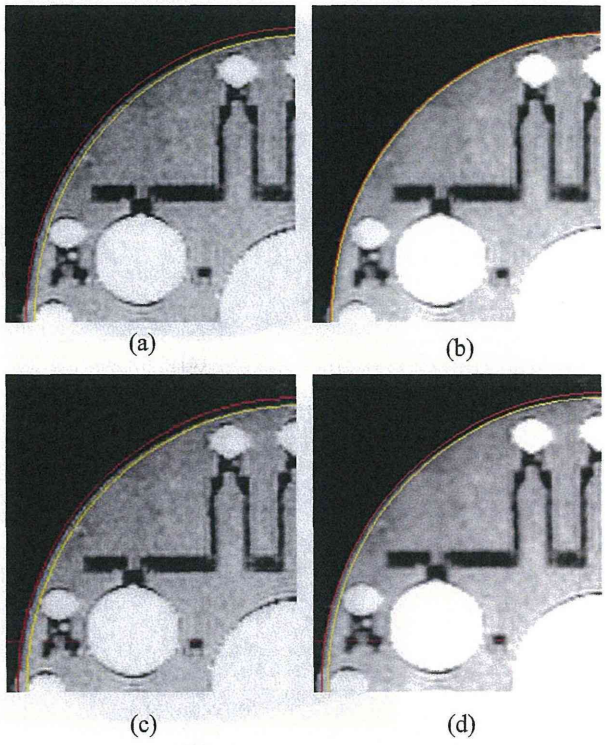

FIG. 2. Phantom across the axial plane. (a) Uncorrected; (b) corrected with the J-ADNI method; (c) GW correction; and (d) GW (nonlinear) and scaling correction (linear). The distance between the yellow and red circles shows the distortion level at the outer shell of the phantom.

For quantitative assessment of our method of correcting phantom images, we calculated the RMS error distribution. The distribution was obtained from uncorrected phantom images and phantom images corrected using Aqual2 and the CR. An incircle and circumcircle were manually drawn on the orthogonal plane of a phantom image (Fig. 4). The median RMS error was 0.615 mm for uncorrected phantom images and 0.257 mm for corrected images. The median CR was 0.985